

Efficient meltwater drainage through supraglacial streams and rivers on the southwest Greenland ice sheet

Laurence C. Smith^{a,1}, Vena W. Chu^a, Kang Yang^a, Colin J. Gleason^a, Lincoln H. Pitcher^a, Asa K. Rennermalm^b, Carl J. Legleiter^c, Alberto E. Behar^{d,2}, Brandon T. Overstreet^c, Samiah E. Moustafa^b, Marco Tedesco^e, Richard R. Forster^f, Adam L. LeWinter^g, David C. Finnegan^g, Yongwei Sheng^a, and James Balog^h

^aDepartment of Geography, University of California, Los Angeles, CA 90095; ^bDepartment of Geography, Rutgers University, Piscataway, NJ 08854; ^cDepartment of Geography, University of Wyoming, Laramie, WY 82071; ^dNASA Jet Propulsion Laboratory, Pasadena, CA 91109; ^eDepartment of Earth and Atmospheric Science, The City College of New York, NY, 10031; ^fDepartment of Geography, University of Utah, Salt Lake City, UT 84112; ^gU.S. Army Cold Regions Research & Engineering Laboratory, Hanover, NH 03755; and ^hEarth Vision Trust, Boulder, CO 80304

Edited by John H. England, University of Alberta, Edmonton, Canada, and accepted by the Editorial Board November 13, 2014 (received for review July 10, 2014)

Thermally incised meltwater channels that flow each summer across melt-prone surfaces of the Greenland ice sheet have received little direct study. We use high-resolution WorldView-1/2 satellite mapping and in situ measurements to characterize supraglacial water storage, drainage pattern, and discharge across 6,812 km² of southwest Greenland in July 2012, after a record melt event. Efficient surface drainage was routed through 523 high-order stream/river channel networks, all of which terminated in moulins before reaching the ice edge. Low surface water storage (3.6 ± 0.9 cm), negligible impoundment by supraglacial lakes or topographic depressions, and high discharge to moulins ($2.54\text{--}2.81$ cm·d⁻¹) indicate that the surface drainage system conveyed its own storage volume every <2 d to the bed. Moulin discharges mapped inside ~52% of the source ice watershed for Isortoq, a major proglacial river, totaled ~41–98% of observed proglacial discharge, highlighting the importance of supraglacial river drainage to true outflow from the ice edge. However, Isortoq discharges tended lower than runoff simulations from the Modèle Atmosphérique Régional (MAR) regional climate model ($0.056\text{--}0.112$ km³·d⁻¹ vs. ~ 0.103 km³·d⁻¹), and when integrated over the melt season, totaled just 37–75% of MAR, suggesting nontrivial subglacial water storage even in this melt-prone region of the ice sheet. We conclude that (i) the interior surface of the ice sheet can be efficiently drained under optimal conditions, (ii) that digital elevation models alone cannot fully describe supraglacial drainage and its connection to subglacial systems, and (iii) that predicting outflow from climate models alone, without recognition of subglacial processes, may overestimate true meltwater export from the ice sheet to the ocean.

Greenland ice sheet | supraglacial hydrology | meltwater runoff | mass balance | remote sensing

Meltwater runoff from the Greenland ice sheet (GrIS) accounts for half or more of its total mass loss to the global ocean (1, 2) but remains one of the least-studied hydrologic processes on Earth. Each summer, a complex system of supraglacial meltwater ponds, lakes, streams, rivers, and moulins develops across large areas of the southwestern GrIS surface, especially below ~1,300 m elevation (3–7), with supraglacial erosion driven by thermal and radiative processes (5). Digital elevation models (DEMs) suggest a poorly drained surface resulting from abundant topographic depressions, which computational flow routing models must artificially “fill” to allow hydrological flow paths extending from the ice sheet interior to its edge (8–11). The realism of such modeled flow paths remains largely untested by real-world observations.

To date, most observational studies of GrIS supraglacial hydrology have focused on large lakes (~1 km²) because of their good visibility in commonly available optical satellite images (6,

12–15). Lakes have also attracted considerable scientific interest because some of them can abruptly drain, rapidly transferring water from the supraglacial to the subglacial system, triggering transient ice uplift and velocity changes (16–20). Greenland’s large supraglacial channels (Fig. 1), however, have received much less study, despite their acknowledged role as a transport mechanism for meltwater and their linkage to englacial/subglacial systems via moulins, crevasses, and shear fractures (21, 22). Reasons for this include difficulties in remote sensing of narrow supraglacial channels (22) and lack of in situ hydraulic data because of challenging field conditions in the ablation zone, where a rapidly lowering ice surface, abundant flowing water, and dangerously fast currents limit mobility and instrument installations. For these reasons, large supraglacial streams are not well characterized, and their overall drainage pattern, storage capacity, discharge, and comparative importance as a GrIS supraglacial runoff mechanism are unknown. In turn, this knowledge gap impedes process-level understanding of ice sheet mass losses from meltwater runoff, which have accelerated since 2000 (2, 23) and are expected to rise further in the future (24–26).

Significance

Meltwater runoff from the Greenland ice sheet is a key contributor to global sea level rise and is expected to increase in the future, but it has received little observational study. We used satellite and in situ technologies to assess surface drainage conditions on the southwestern ablation surface after an extreme 2012 melting event. We conclude that the ice sheet surface is efficiently drained under optimal conditions, that digital elevation models alone cannot fully describe supraglacial drainage and its connection to subglacial systems, and that predicting outflow from climate models alone, without recognition of subglacial processes, may overestimate true meltwater release from the ice sheet.

Author contributions: L.C.S. conceived the project; L.C.S., V.W.C., K.Y., C.J.G., L.H.P., A.K.R., C.J.L., and Y.S. designed research; A.E.B., A.L.L., D.C.F., and J.B. designed instrumentation; L.C.S., V.W.C., K.Y., C.J.G., L.H.P., A.K.R., C.J.L., A.E.B., B.T.O., S.E.M., M.T., R.R.F., A.L.L., and D.C.F. performed field work; V.W.C., K.Y., C.J.G., and L.H.P. conducted analyses; L.C.S. wrote the paper; and V.W.C., K.Y., C.J.G., and L.H.P. helped write the paper.

The authors declare no conflict of interest.

This article is a PNAS Direct Submission. J.H.E. is a guest editor invited by the Editorial Board.

Freely available online through the PNAS open access option.

¹To whom correspondence should be addressed. Email: lsmith@geog.ucla.edu.

²Deceased January 9, 2015.

This article contains supporting information online at www.pnas.org/lookup/suppl/doi:10.1073/pnas.1413024112/-DCSupplemental.

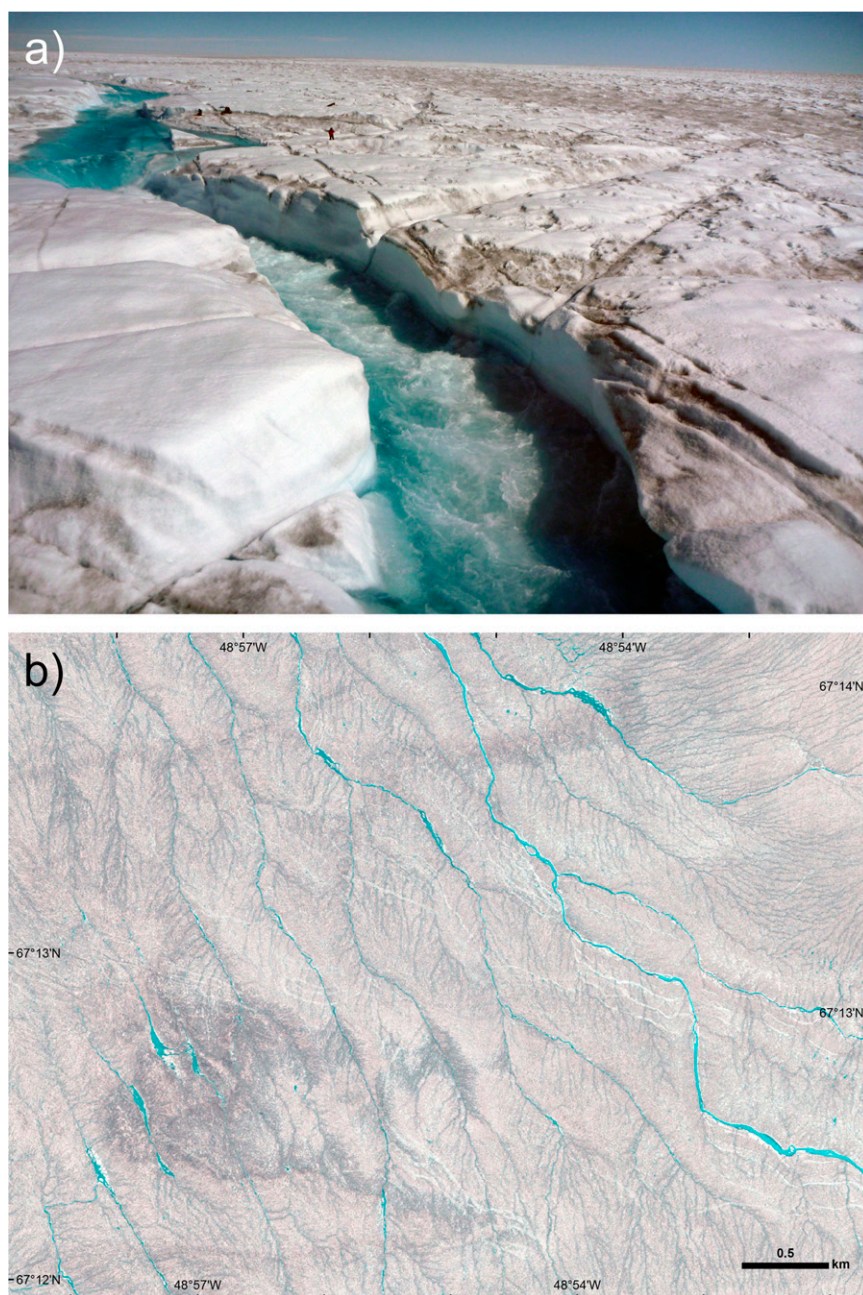


Fig. 1. Supraglacial river networks represent an important high-capacity mechanism for conveying large volumes of meltwater across the GrIS surface, as illustrated by (A) 23 July 2012 field photo (see authors in the image for scale), and (B) same-day WV2 satellite image. Both images were acquired ~55 km inland of the ice edge near Kanqerlussuaq, southwest Greenland.

A possible foreshadow of such a future was a record 11–13 July 2012 melt event that briefly thawed 97% of the GrIS surface (27, 28). Here, we use high-resolution WorldView-2 (WV2) and WorldView-1 (WV1) satellite images, together with contemporaneous in situ field measurements, to study the surface drainage pattern, storage capacity, discharge, and ultimate fate of meltwater generated across a 6,812 km² melt-vulnerable area of the southwest GrIS immediately after this rare event. As such, the goal of the study is to characterize supraglacial drainage conditions for an important runoff-producing region of the ice sheet during peak melting conditions and should be viewed as an end-member situation, rather than as universally descriptive of the broader ice sheet. This area also produces some of Greenland’s largest proglacial rivers (e.g., Isortoq, Watson, Kûk,

Qordlotoq) and offers logistics support from the nearby community of Kangerlussuaq.

During a 6-d mapping period (18–23 July 2012), surface water bodies in this area were mapped at high resolution (2 m) from 32 multispectral WV2 images, all acquired during the peak of the daily melt cycle between 13:53 and 14:09 local time. At the same time, field teams collected supporting in situ hydraulic measurements from nine positions on the ice sheet, including thousands of colocated water depths and spectral reflectances from a customized unmanned surface vessel, flow velocities from drifting autonomous Global Positioning System beacons and portable Doppler radars, cross-sectional velocity fields from an Acoustic Doppler Current Profiler, and channel flow widths, depths, slopes, roughness coefficients, and hydraulic geometry from traditional

Supraglacial Drainage Pattern, Stream/River Networks, and Moulins

The high-resolution mapping derived from the 18–23 July 2012 WV2 multispectral satellite mapping campaign revealed an exceedingly well-drained surface with 523 densely spaced, coalescent supraglacial stream networks characterized by dendritic, parallel, and/or centripetal drainage patterns (Fig. 2). In total, some 5,928 km of large streams were delineated within the WV2 mapped area A_{WV2} , using an automated extraction method (22). Strahler stream orders ranged from 1 to 5, and drainage densities (D_d) ranged from 0.9 to 4.8 km/km², with a weak linear trend of declining D_d with higher elevation. Bifurcation ratios (R_b) averaged 3.7 ± 1.9 , approaching the lower range of terrestrial systems (3.0–5.0) and indicating a homogenous substrate. Inclusion of smaller streams manually digitized within two subcatchments (WV1/2 *Images and Data Processing*; Fig. S3) yields even higher values of stream order (1–6) and D_d (6.0–31.7 km/km²). Such high stream orders for the main-stem channels, together with their high measured velocities (0.2–9.4 m/s), striking blue color, and multiyear stability (Fig. S4), evoke our use of the term “supraglacial river” when referring to these structures, and “supraglacial stream” for their more transient, lower-order feeder tributaries.

All 523 mapped stream/river networks terminated in actively flowing moulins (Fig. 2). The locations of these moulins were geographically dispersed and bore little relation to topographic lows, with 78% lying outside of surface depressions (>0.15 km²), and 92% lying outside of major drained lake basins mapped in Advanced Spaceborne Thermal Emission and Reflection Radiometer satellite imagery (WV1/2 *Images and Data Processing*). The mapped river channels only nominally followed topographic relief, often breaching ice divides. Runoff flowing to lower elevations did not first fill topographic depressions, contrary to a key assumption of terrestrial watershed models [i.e., that depressions must fill with meltwater before overtopping (8, 10)]. Additional manual digitizing of 102 moulins at higher and lower elevations from panchromatic WV1 imagery identifies a weakly inverse relationship between elevation and moulin density, with 16% of river moulins observed to terminate in or near crevasse fields, 3% in drained lake basins, 45% near shear fractures, and 36% displaying no readily visible mechanism for moulin formation (Figs. S1 and S2). Viewed collectively, these observations indicate that DEMs alone cannot fully describe GrIS supraglacial drainage or its moulin connections to englacial/subglacial systems. Finally, laterally draining outlet rivers were observed to flow from all large supraglacial lakes within the A_{WV2} study area, signifying that these prominent features, which would otherwise appear to be impounding meltwater runoff in coarser resolution satellite imagery, presented little obstruction to the lateral passage of meltwater through the supraglacial hydrologic system. In sum, our findings of dense, well-integrated surface drainage pattern, little to no retention in lakes and topographic depressions, and 100% river termination in moulins signify that the surface drainage system was efficiently routing newly generated meltwater to the subsurface in the days after the 2012 melt event.

Supraglacial Meltwater Depth, Storage, and Discharge

Water depths of all supraglacial streams, rivers, ponds, and lakes mapped within the 5,328 km² WV2 study area A_{WV2} were derived at 2-m resolution from field-calibrated WV2 reflectance, after atmospheric correction and an optimal band ratio analysis (29). The fractional area covered by surface water totaled 72.7 km² (1.4% of A_{WV2}), with typical depths ranging from 0.6 to 3.4 m and a mean depth of 2.0 m. Spatial summation of these high-resolution water depth data yields a total supraglacial storage estimate of 0.19 ± 0.05 km³ liquid water by volume (equivalent to 3.6 ± 0.9 cm average depth across A_{WV2}) for the 18–23 July 2012 mapping period.

A field-calibrated hydraulic geometry relationship relating instantaneous supraglacial river discharge (Q_S) to its wetted surface flow width was also applied to the WV2 map, enabling Q_S retrievals at thousands of locations along the delineated river networks. Immediately upstream of each river's terminal moulin, a subset of these Q_S retrievals was spatially averaged within a 1,000-m moving window (along single-thread river reaches only), to obtain 523 moulin discharge estimates ranging from 0.36 to 17.72 m³·s^{−1} (3.56 m³·s^{−1} uncertainty), with a mean value of 3.15 m³·s^{−1} (*Supraglacial Channel Hydraulics and Discharge Estimation*; Fig. S6). A comparison of multitemporal Q_S retrievals from two overlapping WV2 orbit tracks shows that stable flow conditions were preserved between satellite acquisitions (Fig. S7). Summation of these derived discharges across the entire mapped study area A_{WV2} yields a total moulin flux envelope (including uncertainty) of 0.135–0.150 km³·d^{−1} (or 2.54–2.81 cm·d^{−1}) injected into the ice sheet.

The large magnitude of this supraglacial river flux dwarfs observed supraglacial water storage. It is equivalent, for example, to refilling every mapped lake, pond, stream, and river within the 5,328 km² A_{WV2} study area (WV2 volume estimate 0.19 ± 0.05 km³) in just 0.9–1.8 d. Such a discrepancy between low observed supraglacial storage capacity and large observed supraglacial river flux again signifies the efficient evacuation of meltwater through well-organized, hydraulically efficient stream/river channel networks.

Comparison of Field and Remotely Sensed Observations with Runoff Estimates from the MAR Regional Climate Model

The broader importance of this large observed supraglacial river flux becomes apparent when compared with surface mass balance-based estimates of melt production (M) and surface runoff (R) from the MAR regional climate model and a longer record of observed proglacial discharges (Q_P) collected for the Isortoq, a major oceangoing proglacial river that emerges from the ice edge downstream of the study area (with 138 observations acquired between 23 July 2011 and 1 August 2013). In addition to providing some relative context for the 18–23 July supraglacial discharge conditions, the Q_P time series also provides a longer, independent test of the standard practice of using regional climate models to infer GrIS meltwater outflow to the global ocean (and thus one component of its net contribution to sea level rise, after precipitation and refreezing are considered). A comparison of Q_P and R , for example, may yield useful insight about possible englacial/subglacial water storages within the ice sheet, a process not currently recognized in regional climate models.

During the 18–23 July 2012 study period, MAR simulations of R averaged 0.168 km³·d^{−1} (or 3.16 cm·d^{−1} average water depth) across A_{WV2} . This signifies that supraglacial river networks were transporting 76–83% modeled ice sheet runoff R within A_{WV2} and were, thus, effective conduits for the evacuation of meltwater produced on the GrIS surface. Within the smaller 2,574 km² mapped subarea of the Isortoq watershed A_M , the total WV2 moulin flux envelope was 0.021–0.026 km³·d^{−1}, rising to 0.046–0.054 km³·d^{−1} if the aforementioned mean moulin discharge of 3.15 m³·s^{−1} is applied to 98 additional moulins mapped in WV1 imagery (black circles, Fig. 2). Downstream, proglacial discharge Q_P averaged 0.056–0.112 km³·d^{−1} (given the uncertainty of the photogrammetric method). Therefore, despite draining just 52% of the Isortoq river's activated ice watershed A_I , the supraglacial river moulins mapped in A_M were supplying 41–98% of its proglacial discharge, representing a significant conduit linking the interior GrIS ablation surface to subglacial, proglacial, and oceanic systems.

This efficient meltwater release was not evident from June to early July 2012, when proglacial outflow Q_P displayed minimal response to upstream M and R over its activated watershed

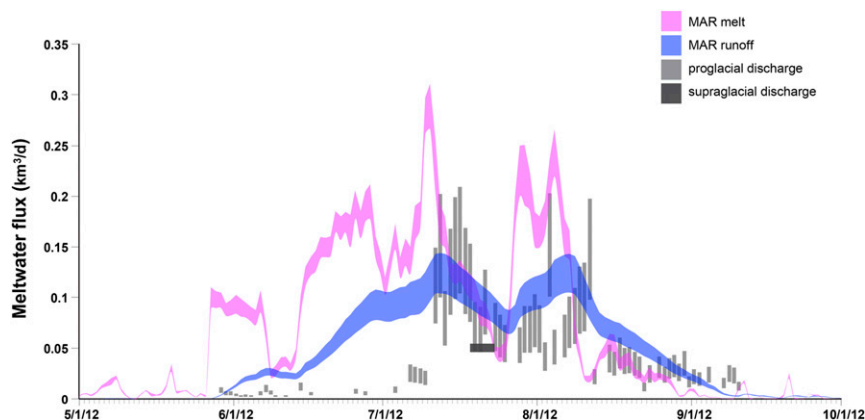


Fig. 3. Comparison of 2012 simulated meltwater production M (magenta) and runoff R (blue) from the MAR regional climate model, observed proglacial discharge (outflow) exiting the ice sheet in the Isortoq river (vertical gray bars, spanning measurement uncertainty), and total supraglacial river moulin discharge estimated for ~52% of the Isortoq ice watershed during 18–23 July 2012 (dark gray box, spanning measurement uncertainty). Observed proglacial outflows are lower than MAR modeled runoff, especially in June. A record melt on the ice sheet occurred 11–13 July 2012.

surface, despite substantial increases in both (Fig. 3). One explanation for this may be temporary water retention in wet snow and slush, which is often observed in early-season satellite imagery (22) (Fig. S4). However, this effect is transient, with supraglacial stream/river networks in this area of southwest Greenland observed to be up and running by 15 July every year examined (e.g., 2012, 2013, and 2014; *Water Depth and Storage Estimation*; Fig. S4). The associated water deficit did not appear in Isortoq in subsequent weeks or the following spring. Integrating Q_P over the full melt season (9 May–10 September 2012) yields a total observed outflow volume that is lower than the corresponding volume of MAR modeled runoff R (i.e., 2.68–5.41 km³ vs. 7.20 km³, or 37–75%). Similarly, temporally interpolated Q_P over the maximum data collection period (23 July 2011–1 August 2013) totaled 4.42–8.93 km³ for observations vs. 10.90 km³ for MAR (41–82%). Even assuming maximum watershed uncertainty (*Isortoq Discharge and Watershed Delineation*; Fig. S8), the integrated Q_P over this period is 8.65–11.98 km³ (37–103%) of MAR runoff. Alternate calculations with no interpolation of daily Q_P yields comparable results (*MAR Regional Climate Model*). This discrepancy between observed Q_P and modeled R suggests that either MAR overpredicts surface melting (an explanation not supported by our in situ ablation-stake measurements; *MAR Regional Climate Model*) or, more likely, that subglacial water retention processes were at play (30); for example, moulin connections to unchanneled parts of the subglacial hydrologic system (31), perhaps interrupted by dynamic switching from cavity to channel basal flow mode (18). Either explanation, especially for such a well-drained, melt-prone area of the ice sheet (13) in an unusually warm year (15), conservatively suggests that runoff simulations from atmospheric models alone, without consideration of englacial/subglacial storages, may overestimate true, ongoing outflow in other colder, snowier parts of Greenland as well.

The extreme 2012 melt event, however, established reasonable convergence between modeled Isortoq watershed R and observed proglacial discharge Q_p (Fig. 3). By 11 July, proglacial discharge rose in the Isortoq River (and also in the Watson River ~13 km to the south, where record flooding destroyed a major bridge in Kangerlussuaq), reaching a peak discharge envelope of 0.104–0.209 $\text{km}^3 \cdot \text{d}^{-1}$ on 16 July. During the 18–23 July mapping period, there was approximate congruence between Q_p (0.056–0.112 $\text{km}^3 \cdot \text{d}^{-1}$) and R (0.081–0.111 $\text{km}^3 \cdot \text{d}^{-1}$), attributed in part to supraglacial river fluxes from ~52% of its watershed (0.045–0.054 $\text{km}^3 \cdot \text{d}^{-1}$). Thereafter, Q_p continued to track R timing for the remainder of the melt season, although at a slightly lower

level (Fig. 3). This general agreement between observed Q_p and corresponding upstream modeled R lends qualitative support to the use of atmospheric models to estimate oceangoing discharge during highly developed drainage conditions, such as occurred here after the 2012 melt event and may become more pervasive in the future (25, 26).

On a deeper level, this research highlights the importance of hydrological processes for inclusive understanding of meltwater losses from melt-prone areas of the GrIS. Our observations show that supraglacial stream/river networks are powerful evacuators of water generated from surface melting, and in the days after the extreme 2012 melt event, neither topographic depressions on the ice surface, supraglacial lakes, nor subglacial storage presented serious obstacles to the efficient transfer of this water toward the bed and proglacial zone. Whether the extent and density of the stream/river networks mapped here were also extraordinary warrants further study, but visual inspection of eight other WV1/WV2 images from other times and years strongly suggests that the processes reported here are recurrent and annual (Fig. S4). Dynamic models of ice flow should therefore consider the injection of large water and heat fluxes through supraglacial river moulins (16, 21, 32), which, this study suggests, can only be mapped through high-resolution remote sensing. Finally, these unusual stream systems invite theoretical study from the broader river modeling/fluviol geomorphology community, in addition to glaciologists interested in process-level understanding of meltwater mass losses from the ice sheet.

With regard to GrIS mass losses, a direct comparison between modeled MAR runoff and gravity recovery and climate experiment (GRACE) gravity anomalies cannot be made for the narrow Isortoq watershed, but a similar discrepancy between regional climate model runoff simulations and GRACE gravity anomalies was evident in Greenland's southwest sector over the period 2002–2010 [i.e., -66 Gt/y surface mass balance vs. -45 ± 8 Gt/yr for GRACE (table 2 in ref. 33)]. This lends further support to our contention that model-based runoff estimates may be higher than true outflow for this important runoff-producing region of the ice sheet, especially in June. Runoff assessments based on regional climate model output should thus consider additional, time-varying retention of meltwater in englacial/subglacial systems or risk overestimating true Greenland meltwater outflow to proglacial areas and the global ocean.

ACKNOWLEDGMENTS. This research is dedicated to the memory of Dr. Alberto Behar, who tragically passed away January 9, 2015. This research

was supported by the NASA Cryosphere Program (Grant NNX11AQ38G), managed by Dr. Thomas Wagner. P. Morin and C. Porter of the Polar Geospatial Center, University of Minnesota, provided WorldView-2 satellite images, tasking, and code for data processing. Updated surface and basal topography datasets were kindly provided by I. Howat (Ohio State

University) and J. Bamber (University of Bristol). Careful, constructive reviews by the external readers led to substantial improvements in the finished manuscript. Field logistical support was provided by CH2M Hill Polar Field Services, the Kangerlussuaq International Science Station, and Air Greenland.

1. van den Broeke M, et al. (2009) Partitioning recent Greenland mass loss. *Science* 326(5955):984–986.
2. Enderlin EM, et al. (2014) An improved mass budget for the Greenland ice sheet. *Geophys Res Lett* 41:866–872.
3. Liang Y-L, et al. (2012) A decadal investigation of supraglacial lakes in West Greenland using a fully automatic detection and tracking algorithm. *Remote Sens Environ* 123:127–138.
4. Colgan W, et al. (2011) An increase in crevasse extent, West Greenland: Hydrologic implications. *Geophys Res Lett* 38:1–7.
5. McGrath D, Colgan W, Steffen K, Lauffenburger P, Balog J (2011) Assessing the summer water budget of a moulin basin in the Sermeq Avannarleq ablation region, Greenland ice sheet. *J Glaciol* 57:954–964.
6. Joughin I, et al. (2013) Influence of ice-sheet geometry and supraglacial lakes on seasonal ice-flow variability. *Cryosph* 7:1185–1192.
7. Lampkin DJ, VanderBerg J (November 20, 2013) Supraglacial melt channel networks in the Jakobshavn Isbræ region during the 2007 melt season. *Hydrol Process*, 10.1002/hyp.10085.
8. Arnold NS (2010) A new approach for dealing with depressions in digital elevation models when calculating flow accumulation values. *Prog Phys Geogr* 34:781–809.
9. Lewis SM, Smith LC (2009) Hydrologic drainage of the Greenland Ice Sheet. *Hydrol Processes* 23:2004–2011.
10. Banwell AF, Arnold NS, Willis IC, Tedesco M, Ahlström AP (2012) Modeling supraglacial water routing and lake filling on the Greenland Ice Sheet. *J Geophys Res* 117: F04012.
11. Bamber JL, Siegert MJ, Griggs JA, Marshall SJ, Spada G (2013) Paleofluvial megacanyon beneath the central Greenland ice sheet. *Science* 341(6149):997–999.
12. Box JE, Ski K (2007) Remote sounding of Greenland supraglacial melt lakes: Implications for subglacial hydraulics. *J Glaciol* 53:257–265.
13. Selmes N, Murray T, James TD (2011) Fast draining lakes on the Greenland Ice Sheet. *Geophys Res Lett* 38:1–5.
14. Leeson AA, et al. (2013) A comparison of supraglacial lake observations derived from MODIS imagery at the western margin of the Greenland ice sheet. *J Glaciol* 59: 1179–1188.
15. Fitzpatrick AAW, et al. (2014) A decade (2002–2012) of supraglacial lake volume estimates across Russell Glacier, West Greenland. *Cryosph* 8:107–121.
16. Catania GA, Neumann TA, Price SF (2008) Characterizing englacial drainage in the ablation zone of the Greenland ice sheet. *J Glaciol* 54:567–578.
17. Das SB, et al. (2008) Fracture propagation to the base of the Greenland Ice Sheet during supraglacial lake drainage. *Science* 320(5877):778–781.
18. Schoof C (2010) Ice-sheet acceleration driven by melt supply variability. *Nature* 468(7325):803–806.
19. Palmer S, Shepherd A, Nienow P, Joughin I (2011) Seasonal speedup of the Greenland Ice Sheet linked to routing of surface water. *Earth Planet Sci Lett* 302:423–428.
20. Sundal AV, et al. (2011) Melt-induced speed-up of Greenland ice sheet offset by efficient subglacial drainage. *Nature* 469(7331):521–524.
21. Phillips T, Rajaram H, Colgan W, Steffen K, Abdalati W (2013) Evaluation of cryo-hydrologic warming as an explanation for increased ice velocities in the wet snow zone, Sermeq Avannarleq, West Greenland. *J Geophys Res Earth Surf* 118:1241–1256.
22. Yang K, Smith LC (2013) Supraglacial streams on the Greenland Ice Sheet delineated from combined spectral – shape information in high-resolution satellite imagery. *IEEE Geosci Remote Sens Lett* 10:801–805.
23. Rignot E, Velicogna I, van den Broeke MR, Monaghan A, Lenaerts JTM (2011) Acceleration of the contribution of the Greenland and Antarctic ice sheets to sea level rise. *Geophys Res Lett* 38:1–5.
24. Alley RB, Clark PU, Huybrechts P, Joughin I (2005) Ice-sheet and sea-level changes. *Science* 310:456–60.
25. Fettweis X, et al. (2013) Estimating the Greenland ice sheet surface mass balance contribution to future sea level rise using the regional atmospheric climate model MAR. *Cryosph* 7:469–489.
26. Vizcaino M, Lipscomb WH, Sacks WJ, van den Broeke M (2014) Greenland Surface Mass Balance as Simulated by the Community Earth System Model. Part II: Twenty-First-Century Changes. *J Clim* 27:215–226.
27. Hall DK, et al. (2013) Variability in the surface temperature and melt extent of the Greenland ice sheet from MODIS. *Geophys Res Lett* 40:1–7.
28. Tedesco M, et al. (2013) Evidence and analysis of 2012 Greenland records from spaceborne observations, a regional climate model and reanalysis data. *Cryosph* 7: 615–630.
29. Legleiter CJ, Tedesco M, Smith LC, Behar E, Overstreet BT (2014) Mapping the bathymetry of supraglacial lakes and streams on the Greenland ice sheet using field measurements and high-resolution satellite images. *Cryosph* 8:215–228.
30. Rennermalm AK, et al. (2013) Evidence of meltwater retention within the Greenland ice sheet. *Cryosph* 7:1433–1445.
31. Andrews LC, et al. (2014) Direct observations of evolving subglacial drainage beneath the Greenland Ice Sheet. *Nature* 514(7520):80–83.
32. Zwally HJ, et al. (2002) Surface melt-induced acceleration of Greenland ice-sheet flow. *Science* 297(5579):218–222.
33. Sasgen I, et al. (2012) Timing and origin of recent regional ice-mass loss in Greenland. *Earth Planet Sci Lett* 333-334:293–303.

Supporting Information

Smith et al. 10.1073/pnas.1413024112

SI Materials and Methods

WV1/2 Images and Data Processing. Multispectral WV2 images over the study area were tasked from DigitalGlobe Inc. through the University of Minnesota Polar Geospatial Center. In total, 32 WV2 images covering 5,328 km² (labeled A_{WV2} in Fig. 2) were acquired 18–23 July after the record melt event that transpired on 11–13 July (1–5), as follows: 18 July (three images, 15:53 GMT, catalog ID 103001001AAC8500), 21 July (11 images, 15:43 GMT, catalog ID 103001001B781900), and 23 July (18 images, 16:08 GMT, catalog IDs 103001001A3C0300 and 103001001A49F200). These images enabled maximum coverage of supraglacial river networks; that is, those networks sufficiently distant from low-elevation, ice-marginal crevasse fields, yet centrally located in an area of abundant supraglacial meltwater (6, 7). Concurrent field team deployments to nine locations on the ice sheet were conducted with day charters on 20, 21, and 23 July, and an ice camp operated 19–24 July 2012. Images were orthorectified, using code developed by the Polar Geospatial Center and the Greenland Ice Mapping Project DEM (8), and then atmospherically corrected using ENVI fast line-of-sight atmospheric analysis of hypercubes. This study focuses on the midelevation ablation zone, so it is unaffected by the low intrinsic resolution of the Greenland Ice Mapping Project DEM at higher elevations. The orthorectified WV2 products offer high spatial resolution (2.0 m) and good horizontal geolocation accuracy (5.4 m). To produce raster surface water masks and vector centerlines of supraglacial river networks, the automated method of Yang and Smith (9) was slightly modified to use a band ratio of Band 2 (blue, 450–510 nm) to Band 8 (near infrared, 860–1,040 nm), with a ratio threshold set to 1.25 and a minimum area threshold of 500 pixels for slush removal. Abrupt river terminations were recorded as moulins (total, 584, with some of the 523 networks having more than one) after visual confirmation in the native WV2 imagery. Intersection of moulin locations with the Greenland Ice Mapping Project DEM identified 458 (78%) as lying outside of topographic depressions (defined as >0.15 km²) and 537 (92%) as lying outside of 23 manually digitized large drained lake scars.

Locations of 102 additional river moulins lying outside of the A_{WV2} mapping area but inside the 30-m potentiometric Isortoq ice watershed A_I (*Isortoq Discharge and Watershed Delineation*) were obtained for a 1,484 km² area through manual mapping from panchromatic WV1 images, thus raising the total satellite-mapped study area to 6,812 km². In total, 20 WV1 images were acquired on 20, 21, 25, 30, and 31 July and 20 August from the Polar Geospatial Center, as follows: 20 July (one image, 16:19 GMT, catalog ID 103001001A50A800), 21 July (four images, 15:24 GMT, catalog IDs 102001001C6DE000, 102001001C131100, 102001001B447700, and 102001001CCA9F00), 25 July (six images, 15:29 GMT, catalog IDs 102001001C9B7500 and 102001001A923A00), 30 July (two images, 15:12 GMT, catalog ID 102001001DDE8400), 31 July (four images, 14:49 GMT, catalog IDs 102001001D0FAB00 and 102001001D407300), and 12 August (three images, 15:05 GMT, catalog ID 102001001CC6B300). Moulin coordinates were digitized in ArcGIS, with attention paid to larger rivers that would have been detected in the WV2 automated algorithm and keeping a consistent scale. This additional mapping increased the total mapped area of the Isortoq watershed to 2,574 km², or 52% of its activated (i.e., runoff-producing) watershed area during the period 18–23 July 2012. Finally, all 179 terminal river moulins mapped within the Isortoq watershed were visually examined in the raw WV1/2 satellite imagery and assigned to

one of four likely mechanisms of moulin formation (crevasse field, shear fracture, lake drainage, undetermined) (Fig. S1). Of 179 moulins mapped within the Isortoq watershed, these assignments were as follows: 28 (16%) river moulins were observed to terminate in or near crevasse fields, 80 (45%) in shear fractures, 6 (3%) in drained lake basins, and 65 (36%) displayed no readily visible mechanism for moulin formation. These categories were then coded as attribute data in ArcGIS and plotted as a function of ice surface elevation (Fig. S2).

Vectorized supraglacial river networks were characterized, using traditional watershed morphometry metrics (10–12) to characterize drainage organization, substrate homogeneity, and surface dissection. These metrics were Strahler stream order, with minimum detected tributaries set to one (11, 12), bifurcation ratio R_b (ratio of the number of streams for a given order N_u to the number of streams in the next higher order $N_u + 1$, ref. 10), and drainage density D_d (total stream length divided by basin area, ref. 10), determined upstream of each terminal moulin basin. For the 40 longest river networks, D_d was determined using the convex hull method (13). To calculate the convex hull, visible tributaries were connected with straight lines to form a polygon in which none of the internal angles exceeded 180° (14). Resultant D_d ranged from 0.90 km/km² to 4.75 km/km², with a weakly linear inverse correlation with elevation ($D_d = 7.490 - 0.004 z$; $R^2 = 0.29$; $P = 0.002$). To quantify stream order and drainage density at even finer spatial scales (~1 m or less) than multispectral WV2, two stream drainage networks were manually digitized from a panchromatic WV1 image acquired on 23 July 2012 (catalog ID 103001001A49F200), centered at 67°12'26"N, 49°5'35"W, and 67°10'45"N, 48°59'1"W, respectively (Fig. S3). Both stream networks were subjected to similar morphometry analysis as the larger WV2 river networks, yielding Strahler stream orders of 1–6 and drainage densities 6.0–31.7 km/km². The well-organized, highly ordered drainage pattern observed for these fine-resolution networks suggests that nearly all small supraglacial streams coalesce into ever-larger ones, ultimately forming the large, multiyear, high-order trunk main-stems (which we propose calling “rivers”) readily visible in WV2 imagery.

Water Depth and Storage Estimation. A total of 8,811 colocated field measurements of water depth and upwelling spectral radiance were collected in two supraglacial rivers and one supraglacial lake with an Oceanscience Z-Boat 1800 unmanned surface vessel custom-fitted with an Ohmex SonarMite 235 KHz echo sounder and Analytical Spectral Devices FieldSpec3 spectroradiometer (15). Water depths were sampled with ± 0.025 m accuracy and a 1 Hz sampling rate. Upwelling radiance was measured from 350 to 1,025 nm with 1-nm resolution and calibrated with a Spectralon reference panel to set integration time, account for instrument dark current, and enable conversion to spectral radiance. The spectrometer fore optic was mounted to a boom extending in front of the unmanned surface vessel, pointed downward at the water surface with a fixed nadir-viewing geometry. Simultaneous downwelling spectral irradiance was continuously recorded on shore by an ASD HandHeld2 spectroradiometer with a cosine receptor oriented skyward. Synchronized time stamps were used to pair all instrument measurements and Global Positioning System positions. All colocated data were used to conduct an optimal band ratio analysis (15) and calibrate a water depth (d) retrieval algorithm for WV2 imagery as $d = 0.895 - 4.33X + 23X^2$ [$r^2 = 0.92$; root-mean-square-error (RMSE) 0.65 m], where $X = \ln(B1/B3)$,

with *B1* as WV2 Band 1 (blue 400–450 nm) and *B3* as WV2 Band 3 (green 510–580 nm). Depth uncertainty was defined as the RMSE from the depth retrieval algorithm (0.65 m). To minimize extreme water depth overestimation from dark cryoconite patches, the upper fifth percentile of retrieved depths was removed. Remaining depth rasters were clipped with the WV2 water mask in ArcGIS and then mosaicked to provide a continuous map of supraglacial surface water depth (2 m posting), with values ranging from 0.7 to 8.1 m and mean depth 2.0 ± 1.4 m. Summation of this map over the water mask, together with associated depth uncertainty (propagated to volume uncertainty), yields an instantaneous supraglacial water volume of 0.19 ± 0.05 km³ integrated over 72.7 km² of mapped surface water area.

Drained lake basin extents were manually digitized from five Advanced Spaceborne Thermal Emission and Reflection Radiometer (ASTER) satellite images acquired 18, 21, and 23 July 2012 (catalog IDs 2119070233, 2119070466, 2119070243, 2119169026, and 2119191938). These data were obtained from the NASA Land Processes Distributed Active Archive Center, USGS/Earth Resources Observation and Science Center. In total, 23 drained lake basins were mapped within A_{WV2} , with areas ranging from 0.2 to 8.4 km², a mean area of 2.1 km², and a total area of 47.3 km².

To assess the multiyear stability of large supraglacial river channels as well as the effect of early-season slush formation and snow clearance from multiyear channels, we examined two WV1 and five WV2 images, with acquisition dates ranging from 6 August 2009 to 19 September 2014 (6 August 2009, catalog ID 10200100075E1200; 12 June 2011, catalog ID 103001000B432900; 25 July 2012, see earlier; 8 August 2013, catalog ID 1030010025219000; 7 July 2014, catalog ID 1030010034A92100; 15 July 2014, catalog ID 1020010030730900; 26 August 2014, catalog ID 1030010036AC6700; and 19 September 2014, catalog ID 10300100350ECD00). As observed in our previous work (9), melt onset initially produces widespread formation of large slush/wet snow patches, which impedes the visible passage of water through multiyear channels. Our examination of these additional images reveals this phenomenon to be transient, with the snow clearance process complete, and supraglacial stream/river drainage systems observed to be freely flowing no later than ~15 July each year, even in 2013 (a cold summer). We therefore conclude that the actively flowing supraglacial drainage conditions reported here, and supraglacial stream/river network establishment more generally, are an annual, recurring event in this area of the southwest GrIS.

Supraglacial Channel Hydraulics and Discharge Estimation. In situ measurements of supraglacial channel flow width, depth, velocity, and slope were measured at 78 cross sections along a ~75-km transect spanning 500–1,400 m above sea level, with measurements taken within ~0–4 h of each satellite overpass. For 54 smaller channels, measurements of flow widths were obtained using extended surveying rods, depths were obtained from a steel probe, and surface velocities were obtained from a FloWav Phaser portable Doppler radar. Water surface slopes were measured over distances of 20 channel widths using a CST/Berger 32X automatic level and surveyor's stadia rod. For 24 cross sections collected longitudinally along three larger rivers (widths, 6–19 m), flow widths, depths, and flow velocities were obtained from a Sontek S5 RiverSurveyor Acoustic Doppler Current Profiler. All measurements were converted to discharge (Q) by the velocity-area method to calibrate an interchannel empirical power-law function relating Q to flow width w (Fig. S5) [$(w = 3.48Q^{0.54}; r^2 = 0.89; \text{RMSE}, 3.11 \text{ m}^3\text{s}^{-1} (16\text{--}19))$]. This purely empirical relationship was observed to be quite stable among the 78 field sites, here attributed to incision of characteristic channel geometry resulting from uniform substrate (ice); lack of alluvial bedforms, bars, or vegetated banks; and a known

codependence between thermal erosion, channel slope, and discharge in meltwater channels (20–22).

The empirical power law was applied to WV2 remotely sensed channel widths throughout A_{WV2} to generate 1,629,502 estimates of supraglacial discharge across the ice sheet. Widths were obtained every 2 m along the river networks, using RivWidth, a software tool to automate calculation of river widths from satellite imagery (23). River path distances (i.e., upstream of a terminal moulin) were computed in ArcGIS. Orthogonal widths spanning multithread channels, wide channels (>20 m), and/or lakes were flagged and excluded from further analysis. Widths from remaining narrow, single-thread channels were converted to Q (by inverting the aforementioned empirical function, $Q = 0.10w^{1.84}$) and averaged longitudinally (24), together with associated uncertainty estimates within continuous 1-km reaches. Total uncertainty in the supraglacial discharge retrievals was determined from both WV2 width measurement uncertainty, $\delta w = \pm 2$ m [$\delta w = 1/2rc$, where r is the sensor spatial resolution and c is the number of banks crossed orthogonally (23)], and RMSE of the empirical power function ($\delta Q_{HG} = 3.11 \text{ m}^3\text{s}^{-1}$). Width uncertainty δw was propagated to discharge uncertainty (δQ_w) as $\delta Q_w = 0.18Q(\delta w/w)$. Discharge uncertainty for each point (δQ) was defined as $\delta Q = \sqrt{(\delta Q_w)^2 + (\delta Q_{HG})^2}$, with reach-averaged uncertainty ($\delta \bar{Q}$) for $\delta Q_1, \dots, \delta Q_n$ discharges within the 1-km reach defined as $\delta \bar{Q} = \sqrt{(\delta Q_1)^2 + \dots + (\delta Q_n)^2}$. Next, the last reach immediately upstream of each moulin was used to estimate meltwater flux. The resultant 523 river moulin discharges ranged from 0.36 to 17.72 m³s⁻¹ (3.56 m³s⁻¹ uncertainty), with a mean value of 3.15 m³s⁻¹, and their frequency histogram is plotted in Fig. S6. All 523 discharge values were summed to produce total moulin discharge, not including uncertainty. Associated uncertainties were combined by taking the square root of the sum of squares to produce a measure of total uncertainty. Total uncertainty provided an envelope around total discharge to produce a total moulin discharge envelope (including uncertainty). This resulted in 1,567–1,730 m³s⁻¹ (or 0.135–0.150 km³d⁻¹) of supraglacial meltwater flux within A_{WV2} penetrating the subglacial system. To assess the stability of flow conditions over the 18–23 July mapping period, cross-sectional discharge retrievals were extracted for five supraglacial river moulins found within a narrow overlapping swath of WV2 data acquired 21 July (15:43) and 23 July (16:08), 2012. Temporal changes were minor (Fig. S7), signifying that flow conditions were similar between the two satellite acquisition dates.

Within the boundaries of the Isortoq 30 m potentiometric watershed delineation (*Isortoq Discharge and Watershed Delineation*), a total of 77 river moulin discharges were retrieved within a 1,090 km² area using field-calibrated WV2, summing to 0.021–0.026 km³d⁻¹. At higher and lower elevations within this watershed, additional discharge within a 1,484 km² area was estimated by applying the mean WV2 flux of 3.15 m³s⁻¹ to 98 moulin locations manually digitized in panchromatic WV1 imagery (102 moulins were mapped, but four were located within ~50 m of each other and drained the same river; *WV1/2 Images and Data Processing*). Discharge uncertainty was also applied to these additional moulins, using the mean WV2 uncertainty of 3.56 m³s⁻¹. Note that these two mapping areas sum to 2,574 km², labeled A_M in the text and Fig. 2, covering 52% of the activated 30 m of potentiometric watershed A_T . Total discharge (including uncertainty) of 0.046–0.054 km³d⁻¹ over A_M was produced in the same manner as for A_{WV2} .

MAR Regional Climate Model. MAR is a regional climate model shown to yield generally reliable simulations of GrIS surface mass balance (3, 25–29). Refreezing is explicitly calculated in the MAR snow model, which calculates vertical profiles of

temperature, density, and liquid water content (30). A fraction of the internal meltwater is retained inside the snow pack, assuming a maximum value for the liquid water content (31). Because of the lack of refreezing observations, modeled refreezing cannot be robustly validated. However, an indication of how well the model performs with respect to refreezing is given by the validation of snow characteristics for single locations with in situ observations (31). MAR represented our own study area well, as confirmed from in situ ablation stake measurements (67.16793 N, 49.65370 W), which averaged $5.09 \text{ cm}\cdot\text{d}^{-1}$ during the study period (18–23 July 2012) compared with $5.59 \text{ cm}\cdot\text{d}^{-1}$ and $4.11 \text{ cm}\cdot\text{d}^{-1}$ for MAR variables M and R , respectively. We note that this agreement is more encouraging than a recent model intercomparison (32), which identified a $\pm 24\%$ MAR error relative to point observations of surface mass balance in the ablation zone. MAR v3.2 outputs of daily melt production and runoff at a 25-km spatial resolution (33) were downloaded from ACADIS Gateway (www.aoncadis.org) and examined over three areas: the entire mapped WV2 mosaic (A_{WV2} , $5,328 \text{ km}^2$), the “activated” Isortoq watershed A_I (i.e., that subarea of the potentiometric ice watershed generating MAR runoff, ranging from 0 to $5,075 \text{ km}^2$ over the Q_p data collection period 23 July 2011–1 August 2013), and a subset of A_I mapped by both WV2 (18–23 July 2012) and WV1 (20 July–12 August 2012) for the purpose of moulin mapping (A_M , $2,574 \text{ km}^2$). To prevent land contamination along the ice edge, only the mean ice-covered MAR data products were used, not mean cell products (which can include mixed pixels). Daily values of M and R for A_{WV2} , A_I , and A_M were calculated by intersection with MAR model output. Fractional MAR grid cells were area-weighted and summed to construct daily time series of M and R over A_I (Fig. 3). A longer daily R time series for A_I was also compared with 138 Isortoq River Q_p observations between 23 July 2011 and 1 August 2013. This comparison was made in two ways: temporal integration with linear interpolation between daily Q_p data gaps, and direct one-to-one comparison between available Q_p and corresponding daily MAR values. The first method yields a total 2012 Isortoq discharge outflow volume of 2.68 km^3 (minimum) to 5.41 km^3 (maximum), compared with 7.20 km^3 total outflow for MAR R . During the complete camera record 23 July 2011–1 August 2013, the corresponding values are 4.42 km^3 (minimum) to 8.93 km^3 (maximum) compared with 10.90 km^3 for MAR (41–82%). The second method averaged respective time series of upper- and lower-bound Q_p estimates over the number of observed daily discharges to produce an average minimum Q_p of $0.022 \text{ km}^3\cdot\text{d}^{-1}$ ($257 \text{ m}^3\cdot\text{s}^{-1}$) and an average maximum Q_p of $0.045 \text{ km}^3\cdot\text{d}^{-1}$ ($518 \text{ m}^3\cdot\text{s}^{-1}$), with no interpolation of missing daily Q_p observations. Average R was computed from daily R for days with Q_p estimates, yielding $0.050 \text{ km}^3\cdot\text{d}^{-1}$ ($574 \text{ m}^3\cdot\text{s}^{-1}$). Thus, both the observed upper and lower bounds of observed proglacial discharge are again overestimated by R , with Q_p averaging 45–90% of R from 23 July 2011 to 1 August 2013.

Isortoq Discharge and Watershed Delineation. Proglacial discharges in the Isortoq River were estimated using field calibrated time-lapse photography of braid plain inundation area (34–37). The method exploits an intrinsic power-law correlation between water surface area and discharge unique to alluvial braided rivers (38, 39), here calibrated from in situ hydraulic measurements collected $\sim 200 \text{ m}$ upstream of the braid plain. The camera system was developed by the Extreme Ice Survey project (www.extremeicesurvey.org) specifically for harsh Arctic weather conditions. System components included a Nikon D200 Digital single-lens reflex camera body, Nikkor lens, modified battery pack, and electronic controller housed in a weatherproof housing with abrasion-resistant polycarbonate window. The housing was mounted on a survey tripod and affixed with bolts and guy wires to a high bedrock ridge overlooking the Isortoq valley floor, with

external power from a 12V gel battery recharged by solar panel. Camera images were acquired every 30 min, yielding a total time series of 21,501 candidate images for discharge estimation between 23 July 2011 and 1 August 2013. MATLAB scripts were written to flag images impacted by fog, blowing dust, shadowing, precipitation, and sun-glint, based on their effect on RGB image histograms. This automated preprocessing step culled the candidate pool from more than 20,000 images to 559 high-quality images collected on 138 d with clear atmosphere, similar time of day, and strong land/water contrast. Training data representing major end member classes (two water classes, two alluvium classes) were manually delineated from a subset of these images and applied to all 559 images to map water surface area, using a supervised maximum likelihood classifier in the ENVI image-processing software. On the basis of 500 manually classified training points, the mean classification accuracy of a 10% sample of classified images of water vs. nonwater was 79.6%. Water classifications were georectified to a 23 September 2011 WV2 image with a $1 \times 1 \text{ m}$ posting. The resulting time series of braid plain inundation area was divided by river reach length (1.22 km) to yield units of effective width W_e (38, 39) and then converted to discharge using in situ measurements of flow surface velocity (float method), width, and depth collected simultaneously with camera images. Measurement uncertainties in the field and camera data were propagated into the discharge retrievals. Because of dangerously fast current, measurement uncertainty was greatest for depth, propagating to significant discharge uncertainty in discharge, as reflected by the use of vertical gray bars in Fig. 3. Upper and lower bounds on proglacial discharge Q_p are provided by rating curves $W_e = 6.16Q_p^{0.82}$ ($r^2 = 0.50$) (upper) and $W_e = 3.46Q_p^{0.82}$ ($r^2 = 0.50$) (lower), respectively. Because diurnal variations in discharge were small in this large river (averaging $0.02 \text{ km}^3\cdot\text{d}^{-1}$, which was one order of magnitude lower than signal), multiple images from the same day were averaged to approximate a single daily value for W_e for each rating curve. The upper and lower limits represent conservative bounds on discharge, incorporating maximum measurement uncertainty when developing each rating curve.

DEMs were used to delineate the Isortoq River's corresponding ice watershed, as the mapped supraglacial river drainage networks were all observed to terminate in moulins well in advance of reaching the ice edge. With no direct way to trace the passage of water under the ice, this leaves either potentiometry (i.e., surface + basal topography to calculate gradients of potentiometric head) or ice surface topography alone (as is done for terrestrial watersheds) as available methods for delineating the broader source watershed for this large proglacial river. Of the two, potentiometry is well grounded in theory and is generally favored by glaciologists (40–42), but the latter approach is occasionally used. The potentiometric equation is $\phi \cong \rho_i g (h_s + 0.1y)$, where ϕ is the hydrostatic pressure potential, ρ_i is the density of ice, g is the gravitational constant, h_s is surface elevation, and y is basal bedrock elevation. Readily available DEMs of surface and basal bedrock topography (8, 43) were used for h_s and y , respectively. After depression filling and manual aggregation of small basin fragments along the ice edge, spatial gradients in ϕ were used to assign flow direction and basin divides, using standard watershed modeling tools in ArcGIS (44–48). For surface-only watershed delineation, basal topography was ignored and flow direction, upstream accumulation area, and divides were generated using standard watershed modeling tools in ArcGIS. Note that these watershed delineation methods are both less straightforward than watershed delineation on land. The potentiometric gradient follows the piezometric (hydrostatic) pressure gradient, driven mainly by ice surface topography (90%) but resultant “Shreve divides,” (i.e., the watershed boundaries generated using the potentiometric equation) may

not necessarily follow surface topography where basal slopes are a factor of 10 (or greater) steeper than surface slopes. Furthermore, our WV2 observations show that supraglacial streams/rivers can sometimes breach ice surface topographic divides. Therefore, it is plausible that supraglacial basins can originate outside of a watershed delineation, and vice versa.

To help quantify the potential effect of such watershed uncertainty on MAR melt (M) and runoff (R) calculations, we delineated six watersheds, using pairings of each method (potentiometric vs. surface) and three surface DEM resolutions (30, 90, and 1,000 m). Because both theory and traditional glaciological practice recommend potentiometry, the uncertainty yielded by this intercomparison is larger than would be incurred by standard practice (and thus believed to be conservative). The analysis

shows that although watershed shapes and areas do vary somewhat between delineation methods and DEM resolutions, the difference is greatest at high elevations, where modeled melt production and runoff are lowest, and smallest at low elevations, where modeled melt production and runoff are highest (Fig. S8). As a result, the associated runoff uncertainty is smaller than the shape/area differences alone would suggest, yielding a range of $0.074\text{--}0.093\text{ km}^3\cdot\text{d}^{-1}$ and $0.081\text{--}0.111\text{ km}^3\cdot\text{d}^{-1}$ for MAR melt and runoff, respectively, during the 18–23 July 2012 study period. These error envelopes are plotted graphically in Fig. 3. For simplicity, elsewhere in the main text, computed fractions are based on our preferred/recommended Isortoq ice watershed, which is the delineation derived by highest-resolution ice surface topography data (30 m) and the potentiometric method (thick magenta line, Fig. S8).

- Nghiem SV, et al. (2012) The extreme melt across the Greenland ice sheet in 2012. *Geophys Res Lett* 39:6–11.
- Bennartz R, et al. (2013) July 2012 Greenland melt extent enhanced by low-level liquid clouds. *Nature* 496(7443):83–86.
- Tedesco M, et al. (2013) Evidence and analysis of 2012 Greenland records from spaceborne observations, a regional climate model and reanalysis data. *Cryosph* 7: 615–630.
- Hall DK, et al. (2013) Variability in the surface temperature and melt extent of the Greenland ice sheet from MODIS. *Geophys Res Lett* 40:1–7.
- Hanna E, et al. (2014) Atmospheric and oceanic climate forcing of the exceptional Greenland ice sheet surface melt in summer 2012. *Int J Climatol* 34:1022–1037.
- Rennermalm AK, et al. (2013) Understanding Greenland ice sheet hydrology using an integrated multi-scale approach. *Environ Res Lett* 8:1–14.
- Chu VW (2014) Greenland ice sheet hydrology: A review. *Prog Phys Geogr* 38:19–54.
- Howat IM, Negrete A, Smith BE (2014) The Greenland Ice Mapping Project (GIMP) land classification and surface elevation data sets. *Cryosph* 8:1509–1518.
- Yang K, Smith LC (2013) Supraglacial streams on the Greenland Ice Sheet delineated from combined spectral – shape information in high-resolution satellite imagery. *IEEE Geosci Remote Sens Lett* 10:801–805.
- Horton RE (1945) Erosional development of streams and their drainage basins; hydrological approach to quantitative morphology. *Bull Geol Soc Am* 56:275–370.
- Strahler AN (1952) Hypsometric (area-altitude) analysis of erosional topography. *Bull Geol Soc Am* 63:1117–1142.
- Strahler AN (1957) Quantitative analysis of watershed geomorphology. *Trans Am Geophys Union* 38:913–920.
- Carr MH, Chuang FC (1997) Martian drainage densities. *J Geophys Res* 102:9145–9152.
- Hoke MRT, Hynek BM (2009) Roaming zones of precipitation on ancient Mars as recorded in valley networks. *J Geophys Res* 114:1–22.
- Legleiter CJ, Tedesco M, Smith LC, Behar E, Overstreet BT (2014) Mapping the bathymetry of supraglacial lakes and streams on the Greenland ice sheet using field measurements and high-resolution satellite images. *Cryosph* 8:215–228.
- Leopold LB, Maddock TJ (1953) The hydraulic geometry of stream channels and some physiographic implications. *US Geol Surv Prof Pap* 252:1–57.
- Kostrzewski A, Zwolinski Z (1995) Hydraulic geometry of a supraglacial stream, Ragnarbræn, Spitsbergen. *Quaest Geogr* 165–176.
- Brykala D (1999) Hydraulic geometry of a supraglacial stream on the Waldemar Glacier (Spitsbergen) in the summer. *Polish Polar Stud* 26:51–64.
- Tabata KK, Hickin EJ (2003) Interchannel hydraulic geometry and hydraulic efficiency of the anastomosing Columbia River, southeastern British Columbia, Canada. *Earth Surf Process Landf* 28:837–852.
- Ferguson RI (1973) Sinuosity of Supraglacial Streams. *Geol Soc Am Bull* 84:251–255.
- Marston RA (1983) Supraglacial stream dynamics on the Juneau icefield. *Ann Assoc Am Geogr* 73:597–608.
- Jarosch AH, Gudmundsson MT (2012) A numerical model for meltwater channel evolution in glaciers. *Cryosph* 6:493–503.
- Pavelsky TM, Smith LC (2008) RivWidth: A Software Tool for the Calculation of River Widths From Remotely Sensed Imagery. *IEEE Geosci Remote Sens Lett* 5:70–73.
- Gleason CJ, Smith LC (2014) Toward global mapping of river discharge using satellite images and at-many-stations hydraulic geometry. *Proc Natl Acad Sci USA* 111(13): 4788–4791.
- Lefebvre F, et al. (2005) Evaluation of a high-resolution regional climate simulation over Greenland. *Clim Dyn* 25:99–116.
- Fettweis X (2007) Reconstruction of the 1979 – 2006 Greenland ice sheet surface mass balance using the regional climate model MAR. *Cryosph* 1:21–40.
- Fettweis X, Tedesco M, van den Broeke MR, Ettema J (2011) Melting trends over the Greenland ice sheet (1958–2009) from spaceborne microwave data and regional climate models. *Cryosph* 5:359–375.
- Tedesco M, Fettweis X (2012) 21st century projections of surface mass balance changes for major drainage systems of the Greenland ice sheet. *Environ Res Lett* 7:045405.
- Fettweis X, et al. (2013) Estimating the Greenland ice sheet surface mass balance contribution to future sea level rise using the regional atmospheric climate model MAR. *Cryosph* 7:469–489.
- Reijmer CH, van den Broeke MR, Fettweis X, Ettema J, Stap LB (2012) Refreezing on the Greenland ice sheet: A comparison of parameterizations. *Cryosph* 6:743–762.
- Lefebvre F (2003) Modeling of snow and ice melt at ETH Camp (West Greenland): A study of surface albedo. *J Geophys Res* 108:4231.
- Vernon CL, et al. (2013) Surface mass balance model intercomparison for the Greenland ice sheet. *Cryosph* 7:599–614.
- Tedesco M, Fettweis X, Alexander PM (2014) MAR v3.2 regional climate model data for Greenland (1958–2013). Available at: www.aoncadis.org/dataset/CPL_MAR.html. Accessed December 19, 2013.
- Ashmore P, Sauks E (2006) Prediction of discharge from water surface width in a braided river with implications for at-a-station hydraulic geometry. *Water Resour Res* 42:1–11.
- Bertoldi W, Zanoni L, Tubino M (2009) Planform dynamics of braided streams. *Earth Surf Process Landf* 34:547–557.
- Bertoldi W, Zanoni L, Tubino M (2010) Assessment of morphological changes induced by flow and flood pulses in a gravel bed braided river: The Tagliamento River (Italy). *Geomorphology* 114:348–360.
- Ashmore P, Bertoldi W, Gardner JT (2011) Active width of gravel-bed braided rivers. *Earth Surf Process Landf* 36:1510–1521.
- Smith LC, Isacks BL, Forster RR, Bloom AL, Preuss I (1995) Estimation of discharge from braided glacial rivers using ERS 1 synthetic aperture radar: First results. *Water Resour Res* 31:1325–1329.
- Smith LC, Isacks BL, Bloom AL, Murray AB (1996) Estimation of discharge from three braided rivers using synthetic aperture radar satellite imagery: Potential application to ungaged basins. *Water Resour Res* 32:2021–2034.
- Shreve RL (1972) Movement of water in glaciers. *J Glaciol* 11:205–213.
- Paterson WSB (1993) *The Physics of Glaciers* (Elsevier Science Ltd, Tarrytown, NY), 2nd Ed.
- Cuffey KM, Paterson WSB (2010) *The Physics of Glaciers* (Academic Press, Burlington, MA), 4th Ed.
- Bamber JL, et al. (2013) A new bed elevation dataset for Greenland. *Cryosph* 7: 499–510.
- Lewis SM, Smith LC (2009) Hydrologic drainage of the Greenland Ice Sheet. *Hydrol Processes* 23:2004–2011.
- Arnold NS (2010) A new approach for dealing with depressions in digital elevation models when calculating flow accumulation values. *Prog Phys Geogr* 34:781–809.
- Banwell AF, Arnold NS, Willis IC, Tedesco M, Ahlström AP (2012) Modeling supraglacial water routing and lake filling on the Greenland Ice Sheet. *J Geophys Res* 117:F04012.
- Bamber JL, Siegert MJ, Griggs JA, Marshall SJ, Spada G (2013) Paleofluvial megacanyon beneath the central Greenland ice sheet. *Science* 341(6149):997–999.
- Banwell AF, Willis IC, Arnold NS (2013) Modeling subglacial water routing at Paakitsoq, W Greenland. *J Geophys Res Earth Surf* 118:1282–1295.

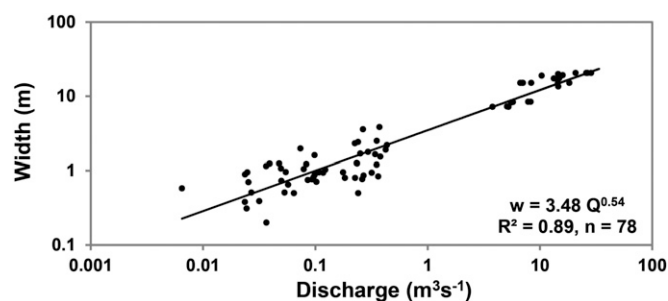


Fig. S5. Field-derived empirical function relating discharge to meltwater channel width for 78 supraglacial stream and river cross sections measured in summer 2012.

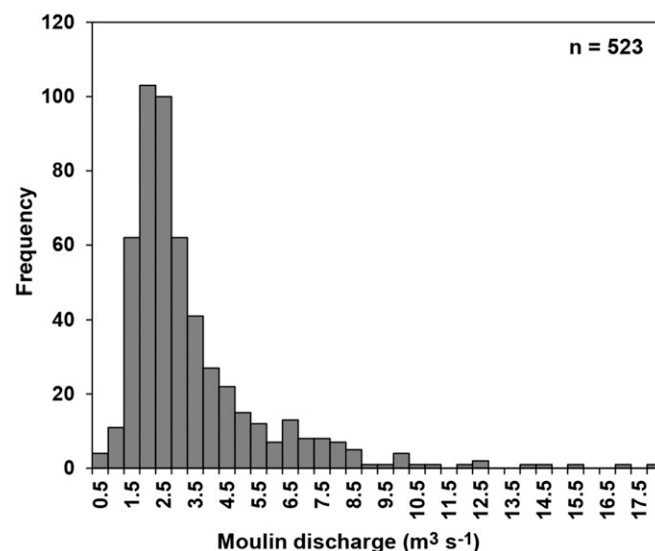


Fig. S6. Frequency histogram of 523 supraglacial river discharges within study area A_{WV2} over the period 18–23 July 2012, retrieved upstream of their respective terminal moulins, using WV2 imagery and the empirical width-discharge relationship presented in Fig. S5.

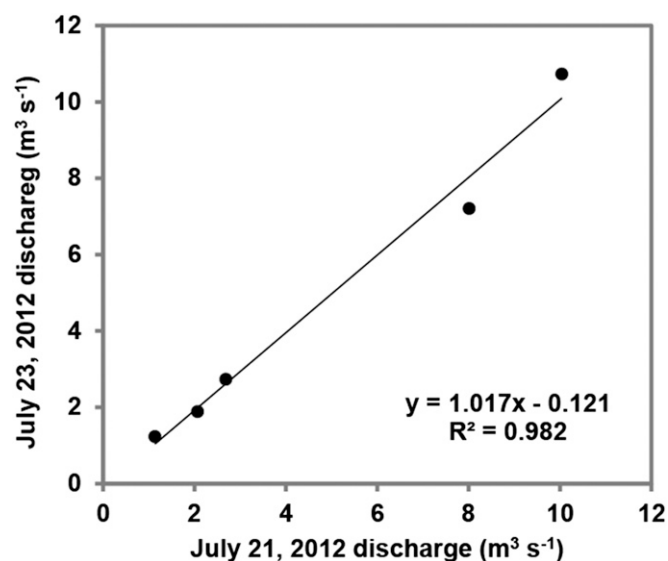


Fig. S7. Comparison of five river moulin discharges retrieved within a narrow overlapping swath of WV2 showed little change between 21 July and 23 July 2012, indicating similar flow conditions between the two dates of acquisition.

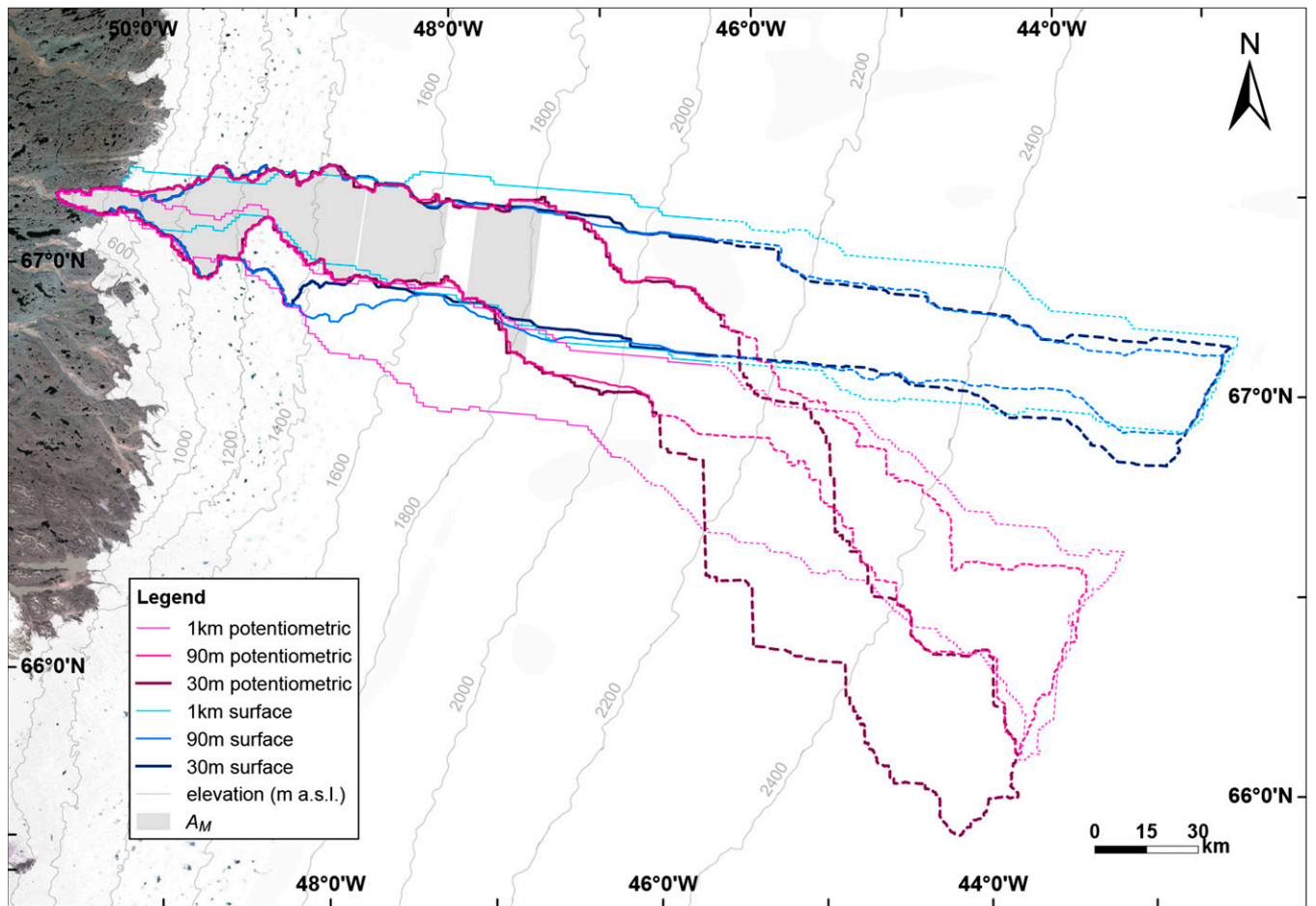


Fig. S8. Six Isortoq watershed delineations created from different pairings of method (potentiometric vs. surface only) and surface DEM resolution (30, 90, and 1,000 m). Solid boundaries delineate thawed, runoff-producing areas over the period 18–23 July 2012 (from MAR). Dashed lines indicate areas that were not generating runoff. The watershed delineations display greatest uncertainty at high elevations, which were not producing runoff and thus had no effect on calculated MAR runoff to the proglacial river Isortoq. Shown in shade is the satellite mapped area A_M , for the recommended 30 m potentiometric basin (thick magenta line).